TELLUS

In situ aerosol characterization at Cape Verde

Part 1: Particle number size distributions, hygroscopic growth and state of mixing of the marine and Saharan dust aerosol

By ALEXANDER SCHLADITZ[1]*, THOMAS MÜLLER[1], ANDREAS NOWAK[1,†], KONRAD
KANDLER[2], KIRSTEN LIEKE[2], ANDREAS MASSLING[1,‡] and ALFRED WIEDENSOHLER[1],
[1]*Leibniz Institute for Tropospheric Research, Permoserstraße 15, 04318 Leipzig, Germany*; [2]*Institute for Applied
Geosciences—Environmental Mineralogy, Technical University Darmstadt, 64287 Darmstadt, Germany*

ABSTRACT

Particle number size distributions and hygroscopic properties of marine and Saharan dust aerosol were investigated
during the SAMUM-2 field study at Cape Verde in winter 2008. Aitken and accumulation mode particles were mainly
assigned to the marine aerosol, whereas coarse mode particles were composed of sea-salt and a variable fraction of
Saharan mineral dust. A new methodical approach was used to derive hygroscopic growth and state of mixing for a
particle size range (volume equivalent) from $dp_{ve} = 26$ nm to 10 μm. For hygroscopic particles with $dp_{ve} < 100$ nm, the
median hygroscopicity parameter κ is 0.35. From 100 nm $< dp_{ve} < 350$ nm, κ increases to 0.65. For larger particles, κ
at $dp_{ve} = 350$ nm was used. For nearly hydrophobic particles, κ is between 0 and 0.1 for $dp_{ve} < 250$ nm and decreases
to 0 for $dp_{ve} > 250$ nm. The mixing state of Saharan dust in terms of the number fraction of nearly hydrophobic
particles showed the highest variation and ranges from 0.3 to almost 1. This study was used to perform a successful
mass closure at ambient conditions and demonstrates the important role of hygroscopic growth of large sea-salt
particles.

1. Introduction

Atmospheric aerosol particles play an important role for the radiative budget of the Earth. The aerosol radiative forcing (RF), which is directly related to the global mean equilibrium temperature at the Earth's surface (Ramaswamy et al., 2001) can be categorized into the direct and indirect effect. The direct effect alters the radiative balance of the Earth's atmosphere by scattering and absorbing short-waved solar and long-waved terrestrial radiation. Numerous research studies (e.g. Forster et al., 2007, and references therein) revealed positive and negative contributions to the direct radiative forcing of, for example anthropogenic haze, biomass burning, mineral dust from desert regions and marine (sulphate and sea-salt) aerosol particles. Nevertheless, the

recent IPCC report (IPCC, 2007) rates the scientific understanding of the direct RF to be medium or even low.

The humidity dependency of aerosol optical properties, for example light scattering is one of the factors, which is crucial to estimate direct RF by aerosol particles. Condensation of water vapour onto particles below super saturation influences strongly their scattering properties (Hänel, 1976) by changing the particle size and refractive index (Covert et al., 1972).

The change of aerosol optical properties along with relative humidity (RH) represents one of the major uncertainties regarding the direct effect of RF. Moreover, the hygroscopic particle growth behaviour is insufficiently implemented in general circulation models (GCM) and is therefore a significant source of uncertainty when predicting RF (Kinne et al., 2003).

However, efforts were undertaken to include effects of hygroscopic growth of aerosol particles in GCMs (Randall et al., 2007). In GCMs, which include radiative transfer, aerosol related processes are treated implicitly, meaning in parametrized form. To model the humidity dependence of light scattering of an aerosol, the parametrized dry particle size distribution as well as the parametrized hygroscopic growth factors of the particles at ambient conditions have to be known (Gysel et al., 2002).

---

*Corresponding author.
e-mail: alexander.schladitz@tropos.de
†Now at: Physikalisch-Technische Bundesanstalt, Bundesallee 100,
38116 Braunschweig, Germany.
‡Now at: National Environmental Research Institute, Aarhus University,
4000 Roskilde, Denmark.

Hygroscopic properties for submicrometre marine aerosols were reported for different locations of the world, for example in the Pacific and Southern Ocean (Berg et al., 1998), eastern Northern Atlantic Ocean (Swietlicki et al., 2000) and Southern Atlantic Ocean and Indian Ocean (Massling et al., 2003). However, field studies of hygroscopic properties of supermicrometre particles are scarce and were carried out by Massling et al., (2007) off the coasts of Japan, Korea and China during the Aerosol Characterization Experiment-Asia with some influence of Asian dust. On the other hand, hygroscopic properties at a Saharan dust source was recently published by Kaaden et al., (2009). Up to now, a comprehensive study of hygroscopic properties of the mixed marine and Saharan dust over the Atlantic Ocean was not done yet.

This paper presents measurements as well as parametrizations of dry particle number size distributions, hygroscopic growth factors and hygroscopic mixing state information of mixed aerosols in the Cape Verde region. The measurements were conducted during winter 2008 with the highest occurrence of spreading dust plumes from the Saharan desert over the Atlantics (Chiapello et al., 1997; Engelstaedter et al., 2006), especially at low altitudes in the trade wind layer (Chiapello et al., 1995).

An overview about the general meteorological situation during the campaign and possible aerosol source regions from trajectory analysis is given in Knippertz et al. (2011).

Hence, from these investigations and from Lidar profiling (Tesche et al., 2009), the impact of biomass-burning aerosol was exclusively detected in higher air layers. Therefore, for the ground-based measurements, the biomass-burning aerosol is not important for this work.

The present comprehensive study comprises a new approach to derive size segregated hygroscopic growth factors and hygroscopic state of mixing (number fraction of hygroscopic and hydrophobic particles) in a large diameter size range from 26 nm up to 10 μm. This method also provides the fractioning between marine (background) and Saharan mineral dust aerosol with a temporal resolution of three hours. The yielded growth factors and dry particle number size distributions were parametrized and were used (e.g. Schladitz et al., 2011) for model calculations concerning humidity effects of aerosol optical properties. Results from single particle analysis were used to identify the hygroscopic inorganic components and compared with the measured hygroscopic growth factors. In addition, the calculated wet particle mass concentration due to hygroscopic growth was compared with the measured total particle mass concentration at ambient conditions.

2. Methods

Here, we briefly introduce the different measurement techniques applied in this study including calibrations, measurements and data processing.

2.1. Location and measurement conditions

The measurements were deployed from January 17 to February 10, 2008 (DOY 17.0–42.0) in the frame of the Saharan mineral dust experiment part 2 (SAMUM-2, Ansmann et al., 2011). The measurement location was near the Praia airport (14°57′N, 23°29′W, 101 m height above sea level) at Santiago Island, Cape Verde.

The experimental setup of all instruments, which are relevant in this work and measured inside a measurement container are shown in Fig. 1. In addition, Table 1 gives an overview of measured and derived quantities, size ranges, type of diameters and RH for each instrument. To supply the instrumentation with aerosol, an aerosol PM_{10} inlet (Rupprecht and Patashnik Co. Inc., Albany, NY, USA) was employed to remove particles larger than 10 μm in aerodynamic diameter ($dp_a < 10$ μm). Downstream of the aerosol inlet, an automatic aerosol diffusion dryer (Tuch et al., 2009) dried the sample aerosol below 30% RH to avoid water uptake of aerosol particles before entering the air-conditioned container. The aerosol diffusion dryer was installed vertically to avoid gravitational losses of larger particles in the sampling line.

Downstream of the dryer and inside the container, the sample aerosol was split isokinetically to conduct the aerosol to various instruments. The mean air temperature inside the container was kept constant (293 ± 2 K), using two independently working air conditioners.

The measured quantities that were measured outside the measurement container are described in Sections 2.6 and 2.7.

2.1.1. General remarks for the measurements and data processing. Corrupted measurements through, for example flow instabilities, zero measurements, calibrations and incorrect measurements for other reasons were removed from the raw data. The Humidifying Differential Mobility Particle Sizer (HDMPS) introduced in Section 2.4 is the instrument with the lowest temporal resolution of three hours. After applying all common corrections described in this section, the data were averaged in time intervals of three hours yielding a uniform data set. The measurement period was from DOY 17–42 where data from most of the instruments were available.

The measured data relate to thermodynamical conditions inside the container. During the campaign, the conditions were stable with only small changes in temperature (293 ± 2 K) and atmospheric pressure (1001 ± 1.6 hPa).

2.2. Dry particle number size distribution

Dry particle number size distributions (PNSDs) were measured in the size range from 26 nm to 10 μm using a Differential Mobility Particle Sizer (DMPS) and an Aerodynamic Particle Sizer (APS model 3321/Serial no. 1297; TSI Inc., St. Paul, MN, USA). The nominal mobility diameter range for the closed loop
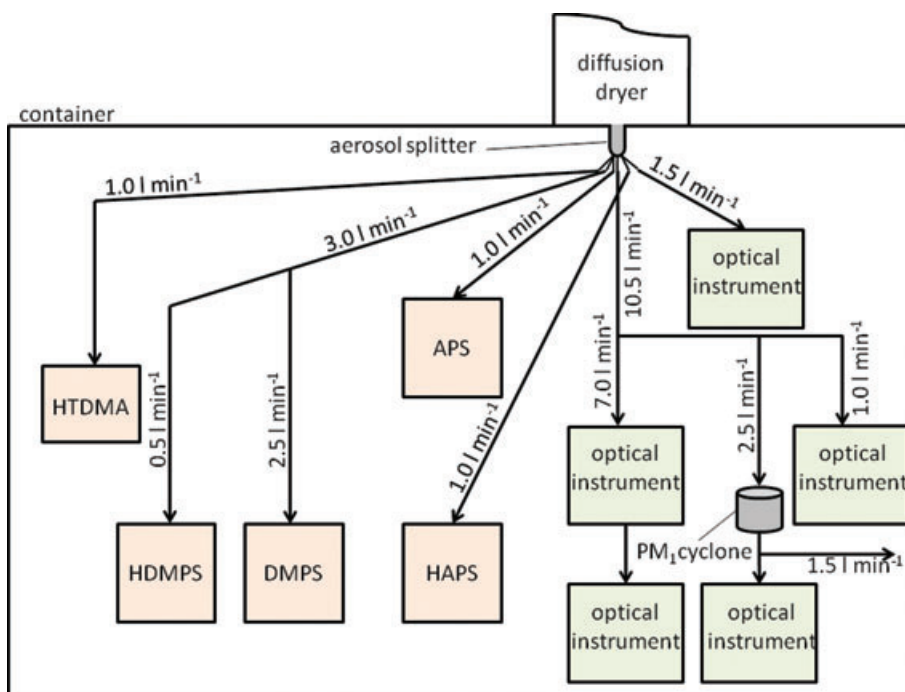
Fig. 1. Instrumental setup of the container and flow rate partitioning to the measurement devices. Instruments for microphysical characterization are shown on the left side (orange boxes), whereas optical instrumentation are described in Schladitz et al. (2011).

Table 1. Overview of instrumentation including information of measured and derived quantities, size ranges, type of diameters and RH

Instrument name	Quantity	Derived quantity	Size range	RH
DMPS	Particle number size distribution	–	Mobility size range from 26 to 800 nm	<30%
APS	Particle number size distribution	–	Aerodynamic size range from 0.835 to 10 μm	<30%
HTDMA	Hygroscopic growth distribution	Volume equivalent hygroscopic growth factors of hygroscopic and hydrophobic particles	Discrete mobility diameters of 30, 50, 80, 150, 250 and 350 nm	85%
HDMPS	Humidified particle number size distribution	Average volume equivalent hygroscopic growth factors	Mobility size range from 26 to 900 nm	30%, 55%, 75% and 90%
HAPS	Humidified particle number size distribution	Average aerodynamic hygroscopic growth factors	Aerodynamic size range from 0.835 to 10 μm	85%

DMPS (Jokinen and Mäkelä, 1997; Birmili et al., 1999) was from $dp_\mathrm{m} = 26$ to 800 nm, whereas the aerodynamic diameter range for the APS was from $dp_\mathrm{a} = 0.835$ to 10 μm.

Because of the lowest selected mobility diameter, the decreasing counting efficiency for particles $dp_\mathrm{a} < 20$ nm for the condensation particle counter (Wiedensohler et al., 1997) was neglected. However, the operated CPC (CPC model 3010/Serial no. 2069, TSI Inc.) worked at the half nominal flow rate (0.5 l min^{-1}). Laboratory measurements showed that the CPC counting efficiency in this case is generally approximately re-

duced by 10% for particles with $dp_m > 26$ nm. The aerosol inlet flow rate was monitored and was always within 2% of the nominal value. Prior to the campaign, the sizing of the DMPS was checked using spherical polystyrene latex particles (PSL) with volume equivalent particle diameters of $dp_\mathrm{ve} = 100, 200$ and 500 nm. During the campaign, the aerosol and sheath airflow rates were daily checked.

The sizing of the APS was checked prior to the campaign using PSL particles with $dp_\mathrm{ve} = 800, 1000$ and 2000 nm that corresponds to $dp_\mathrm{a} = 820, 1025$ and 2050 nm using a PSL

density of $\rho_p = 1050$ kg m^{-3}. The measured PNSD by the APS showed very narrow lognormal size distributions with geometric mean diameters within 2% of the initial PSL particle sizes.

Before the recorded DMPS number concentrations were corrected for multiple charged particles in the APS size range, they were converted to a uniform particle diameter. To combine the DMPS and APS size distribution to one uniform PNSD, the common volume equivalent particle diameter was chosen as a reference particle diameter. In accordance to calculations of optical particle properties in Schladitz et al. (2011), which are based on the findings of this work, the volume equivalent particle diameter is the most suitable one.

Because the DMPS and APS measure particles according to different physical methods, a formula given in DeCarlo et al. (2004) was used that converts volume equivalent to mobility diameters:

$$dp_m = dp_{ve}\chi \frac{C_c(dp_m)}{C_c(dp_{ve})}, \qquad (1)$$

and volume equivalent to aerodynamic diameters

$$dp_a = dp_{ve}\sqrt{\frac{1}{\chi}\frac{\rho_p}{\rho_0}\frac{C_c(dp_{ve})}{C_c(dp_a)}}, \qquad (2)$$

where C_c is the size-dependent Cunningham slip correction, χ is the dynamic shape factor, ρ_p is the dry particle density and ρ_0 is the reference density of 1000 kg m^{-3}. For simplification, it is assumed that in the DMPS size range the particles are spherical, meaning $\chi = 1$. Then, the ratio of the Cunningham slip correction is unity and hence eq. (1) reduces to $dp_{ve} = dp_m$. The APS is measuring in the size range of the continuum regime, where $C_c(dp_{ve}) = C_c(dp_a)$ and hence eq. (2) simplifies to $dp_{ve} = dp_a\rho_{eff}^{-0.5}$ with an effective density $\rho_{eff} = \rho_p(\rho_0\chi)^{-1}$.

Figure 9 shows results from the single particle analysis, which revealed that particles larger than 1 μm mainly consist of Saharan mineral dust and sea-salt (sodium chloride and sodium sulphate). The dry density of Saharan dust particles was determined in a range of $\rho_p = 2450$–2700 kg m^{-3} over the Cape Verde Islands (Haywood et al., 2001) and at a major dust source in southern Morocco (Kaaden et al., 2009; Kandler et al., 2009). The dry particle density of sodium chloride is known to be $\rho_p = 2160$ kg m^{-3}. The dry dynamic shape factor χ of mineral dust is $\chi = 1.25$ (Kaaden et al., 2009) for 1 μm particles, whereas the dynamic shape factor for sodium chloride in the continuum regime is $\chi = 1.08$ (Kelly and McMurry, 1992; Gysel et al., 2002). The overall effective density of the dust and sea-salt fraction is approximately 2. Without any knowledge of the actual mixing state of sea-salt and dust, the aerodynamic diameters were converted into volume equivalent diameters using this effective density of 2.

As proposed by Schladitz et al. (2009), the DMPS number concentration is biased by multiple charged particles (APS size range particles), when the particle number concentration in the

APS size range exceeds 50 cm^{-3}. To remove these multiple charged particles, a procedure described in Birmili et al. (2008) and Schladitz et al. (2009) was used, applying the measured APS number size distribution. The corrected DMPS mobility distributions were then inverted using the regular inversion algorithm that accounts for the multiple charge correction, the specific CPC counting efficiency and the DMA transfer function (Stratmann and Wiedensohler, 1996). Finally, the DMPS and APS data were merged to one final PNSD (volume equivalent diameter) ranging from 26 nm to 10 μm.

The whole size range of the dry PNSD was best represented by four lognormal size distributions. Finally, the time series of the dry PNSD was automatically fitted to lognormal size distributions:

$$\frac{dN}{dlog dp_{ve}} = \sum_{i=1}^{4} \frac{N_i}{\sqrt{2\pi}\log\sigma_{g_i}}\exp\left[-\frac{\left(\log dp_{ve} - \log d_{g_i}\right)^2}{2\left(\log\sigma_{g_i}\right)^2}\right], \qquad (3)$$

using a least square algorithm (Birmili, 1998). The derived fit parameters are the total particle number concentration N, the geometric mean diameter d_g and the geometric standard deviation σ_g for each mode i.

2.3. Hygroscopic growth distribution

To determine the hygroscopic growth distribution for certain particle sizes, we employed a Hygroscopicity Tandem Differential Mobility Analyzer (HTDMA) technique (Liu et al., 1978). A first DMA selects a quasi-monodisperse aerosol, whereas the CPC measures the particle number concentration. Downstream, the quasi-monodisperse aerosol is conditioned to a target RH, typically above the deliquescence point of common inorganic salts in the atmosphere. The subsequent hygroscopic growth distribution of the quasi-monodisperse aerosol is measured by a combination of a second DMA and a CPC. The setup of the HTDMA used here is explained in Massling et al. (2007). During the measurement campaign, hygroscopic growth distributions were determined for particles with dry mobility diameters of $dp_m = 30$, 50, 80, 150, 250 and 350 nm at RH = 85%. The selected RH is an appropriate compromise to guarantee that the most abundant particles exceeded the deliquescence point and hygroscopic growth distributions for the largest initial diameter will completely be measured by the second DMA.

The measurement error of the HTDMA mainly depends on the uncertainty in measuring and controlling the RH within the system (Massling et al., 2011). Therefore, all RH sensors were calibrated with a dew point mirror sensor prior to the measurement campaign. Because of manifold reasons as outlined in Massling et al. (2011), a size shift between the DMAs occurs. The sizing accuracy of the entire HTDMA and a possibly size shift between the DMAs were checked before the campaign by selecting atomized ammonium sulphate particles at RH < 20%. A growth factor correction factor was calculated for each

initial dry diameter employing the inversion toolkit for TDMA measurements (TDMAinv, Gysel et al., 2009). The growth factor correction factor lies in between 0.95 and 1.05, and is defined as the ratio of the initial dry diameter and the peak diameter measured by the second DMA.

Briefly, the volume equivalent hygroscopic growth factor (GF_{ve}) is introduced, which is generally defined as

$$GF_{ve}(RH) = \frac{dp_{ve}(RH)}{dp_{ve}(dry)}. \tag{4}$$

Here, GF_{ve} is the reference hygroscopic growth factor in similarity to dp_{ve} as a reference diameter.

Hygroscopic growth distributions were experimentally determined for initial dry diameters of $dp_{ve} = dp_m = 30, 50, 80, 150, 250$ and 350 nm and evaluated using the TDMAinv inversion toolkit (Gysel et al., 2009). Gysel et al. (2009) explain the necessity to invert TDMA-based measurements. The TDMAinv inverts the measured hygroscopic growth distribution to obtain a normalized growth factor probability density function (GF-PDF). The GF-PDF is defined that the integral over the full GF range equals unity. The inversion algorithm considers the growth factor correction factor described earlier. For the data evaluation, we allowed a tolerance range in RH of 3% to the set point of 85%. In a later stage of data evaluation, the GF-PDF was corrected to the set point RH using eq. (3) from Gysel et al. (2009).

Figure 2 shows an example of a hygroscopic growth distribution and a GF-PDF of an externally mixed aerosol at Cape Verde in terms of hygroscopic growth. The left and right modes show the nearly hydrophobic and hygroscopic particles, respec-

tively. In analogy to Swietlicki et al. (2008), the minimum between the two modes splits the particles into a fraction of nearly hydrophobic particles ($GF_{ve} < 1.2$) and a fraction of hygroscopic particles ($GF_{ve} > 1.2$). The number fractions and their corresponding hygroscopic growth factors of the nearly hydrophobic and hygroscopic particles were determined by integration of the normalized growth factor probability density function (GF-PDF) in defined GF_{ve} ranges.

The HTDMA may classify single as well as multiple charged particles in the same mobility bin. A correction of multiple charged particles selected by the first DMA in the HTDMA is not possible. However, with the simultaneous measurement of the particle number size distribution, the error can be quantified. Duplissy et al. (2009) pointed out, if the fraction of single charged particles in the first DMA is < 80%, the HTDMA data are erroneous and should be excluded from the data set. The rest of the HTDMA data are unexceptional useful. The fraction of single charged particles was determined using the DMPS data and is the ratio of the number concentration of single charged particles to the raw number concentration including single charged as well as multiple charged particles.

Figure 3 illustrates a time series of the fraction of single charged particles for the selected initial dry diameters of the HTDMA. For $dp_{ve} = 150, 250$ and 350 nm and during dust dominated periods DOY 24.5–26.5 LT and 28–34 LT (cf. Fig. 12), the fraction of single charged particles was in the range between 10% and 80%.

The multiple charged particles especially for $dp_{ve} = 150, 250$ and 350 nm can be roughly classified to the coarse particle mode,
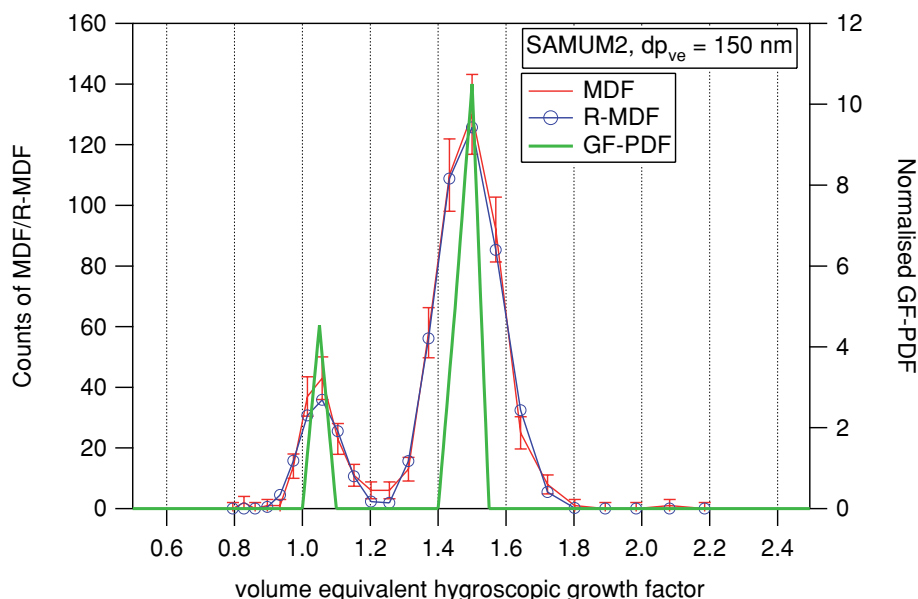

Fig. 2. Typical hygroscopic growth distribution derived from the HTDMA (red solid line). The example shows also the retrieved normalized growth factor probability density function (green solid line) after application of the TDMAinv program for an initial dry diameter of $dp_{ve} = 150$ nm.
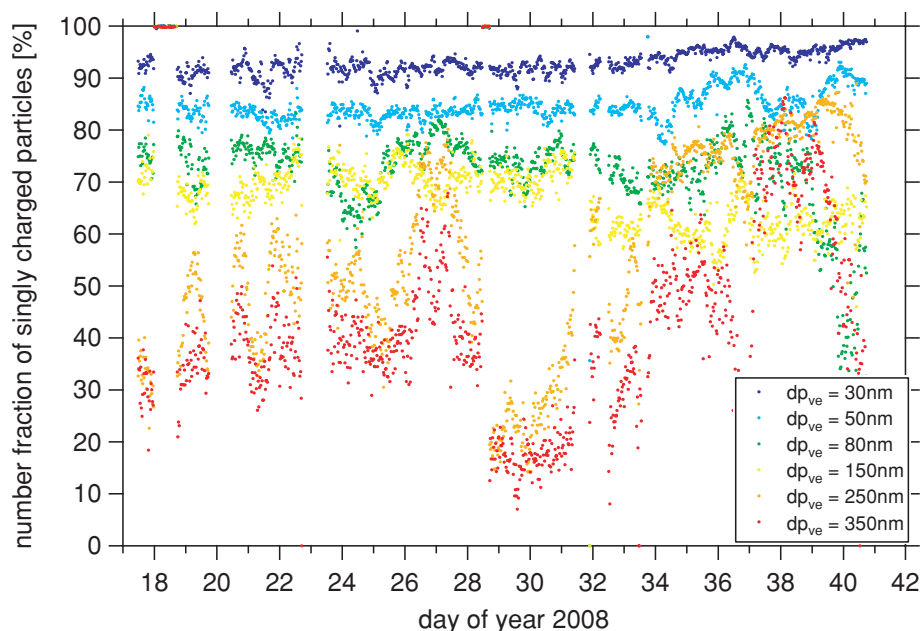
Fig. 3. Time series of the single charged particle fraction deduced from the DMPS for initial dry diameters of dp_{ve} = 30, 50, 80, 150, 250 and 350 nm.

which composed of sea-salt and mineral dust (cf. Section 2.5.2). However, the number concentration of multiple charged particles depends on the number concentration of particles in the coarse particle mode, which was mainly triggered by hydrophobic mineral dust particles.

From the argumentation above it follows that the number fraction of nearly hydrophobic particles is measured higher than in reality. It follows that the number fraction of nearly hydrophobic particles and hence the hygroscopic number fraction are more biased than the respective GF_{ve}. For further analysis, only data of biased number fractions were excluded from the HTDMA data.

2.4. Humidified particle number size distribution

The measurement technique for the humidified PNSD is similar to that for the dry PNSD. The HDMPS measures the PNSD in the size range from 26 to 900 nm for discrete RHs, which can be varied in the range between 30% and 90% RH (Birmili et al., 2009). The size range from 0.835 to 10 μm was measured with a humidified APS (HAPS) to measure the PNSD at a constant RH.

Briefly, the HDMPS works as follows. The entering aerosol is pre-humidified to approximately 90% RH. This process humidifies the particle above the known deliquescence point of the most abundant aerosol species. In a next step, the aerosol is conditioned to the target RH so that the particles remain in a metastable equilibrium with the surrounding moist air.

The time required for a cycle of three PNSD scans at a certain RH is about 30 min. During the measurement campaign,

this cycle was repeated for four different RHs. Adding the time for RH stabilization between each change in RH, the complete characterization of the aerosol across the operated relative humidities of RH = 30%, 55%, 75% and 90% required about 3 h.

Vaisala humidity/temperature sensors are used to monitor temperature and regulate the RH within the systems. They were calibrated prior to the measurement campaign with a dew point mirror sensor. The correct sizing of the HDMPS was calibrated with ammonium sulphate particles at the operated relative humidities as follows.

During the calibration procedure, the HDMPS measured the size distribution of ammonium sulphate particles at 30%, 55%, 75% and 90% RH, whereas the DMPS measured the dry PNSD simultaneously.

Hygroscopic growth factors for ammonium sulphate for each size bin of the dry PNSD was taken from literature (Tang and Munkelwitz, 1994; Tang, 1996). According to eq. (4), the wet diameter and hence the wet PNSD were calculated from the dry PNSD for each RH given above and compared with the measured wet PNSD of the HDMPS. In a last step, size- and RH-dependent correction functions were calculated, which are defined as the ratio of the measured wet PNSD to the calculated wet PNSD. The correction functions include differences between the DMPS and HDMPS with respect to size-dependent counting efficiencies of the CPCs and particle losses in the sampling lines to the DMAs. Figure 4(a) shows arithmetic mean values $\pm$ single standard deviation of four independent HDMPS calibrations performed on January 19, 22, 31 and February 9. There is a significant deviation from unity for
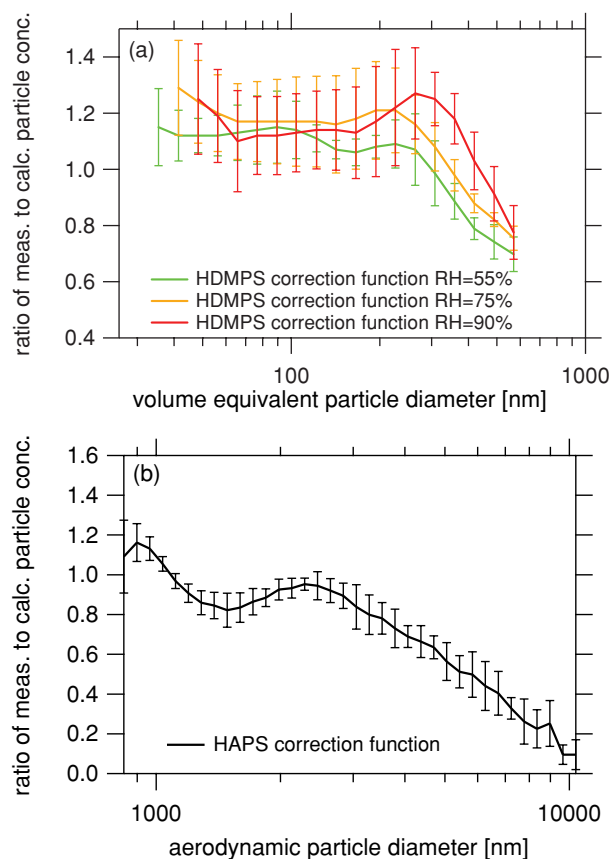
Fig. 4. (a) Size-dependent correction functions for the HDMPS at 55%, 75% and 90% RH. (b) Size-dependent correction function for the HAPS.

$dp_{ve} < 300$ nm. For $dp_{ve} > 400$ nm, the correction functions decrease with increasing particle size and show also a slight RH dependency.

The HAPS is a novel instrument and was constructed prior to the field measurement. The HAPS consists of a humidification unit and an APS (serial no. 1223). Figure 5 shows the design of the HAPS schematically. The humidification unit for the sheath and aerosol air is similar to the HDMPS, except for the pre-humidifier. The mixing of the wet and dry sheath and aerosol air branches to a set point RH of 85% was achieved by manual adjusting the flows via needle valves. Humidity sensors in the HAPS were calibrated prior to the measurement campaign with a dew point mirror sensor. The HAPS calibration was done in the same way as the HDMPS calibration exemplified earlier. Figure 4(b) shows the average size-dependent correction function $\pm$ single standard deviation of four independent HAPS calibrations performed on January 21, 22 and February 3, 10. The correction function includes different counting efficiencies between the two APS, different particle losses in the sampling lines relative to the dry APS, and RH changes of the aerosol inside the HAPS. For $dp_a > 2000$ nm, the correction function decreases, because of the conditioner unit, the sampling path to the HAPS is longer than for the APS and thus causes higher particle losses.

2.5. RH-dependent hygroscopic growth factors and hygroscopic state of mixing

The objective of this section is to derive a time series of RH-dependent hygroscopic growth factors and their corresponding
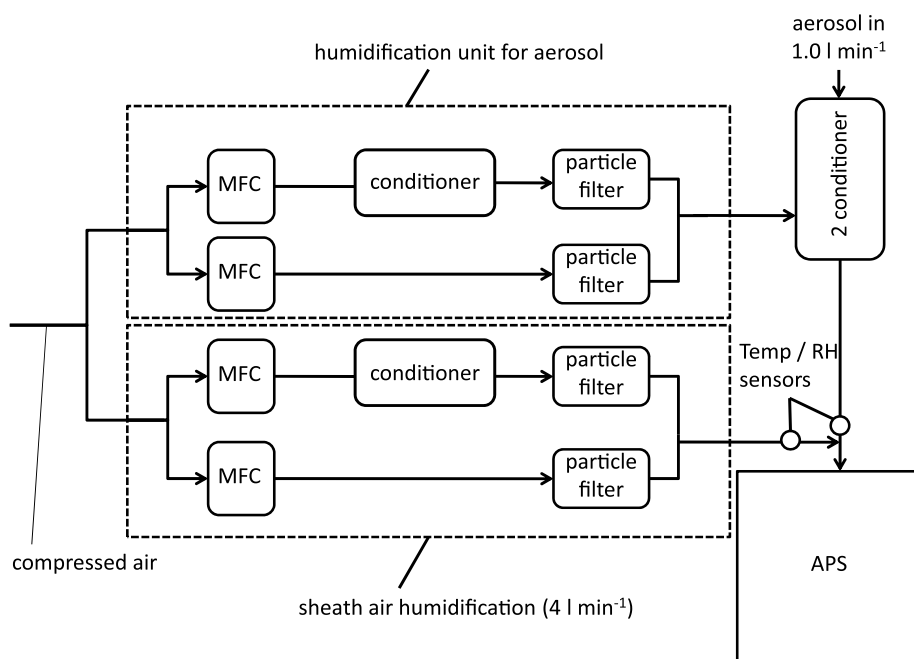

Fig. 5. Schematic design of the HAPS.

number fractions in the volume equivalent size range from 26 nm to 10 μm by using the HDMPS, HAPS and HTDMA data as well as the dry PNSD. To achieve this aim, it was necessary to solve several complex problems:

- The HAPS measured the humidified aerodynamic PNSD. In combination with the aerodynamic PNSD at dry conditions, an average aerodynamic growth factor was derived. Because the volume equivalent diameter is the reference diameter for the hygroscopic growth factor, a conversion from the aerodynamic to the volume equivalent hygroscopic growth factor had to be carried out.

- HTDMA data deliver the hygroscopic state of mixing quasi-continuously in the size range from $dp_{ve} = 30$ to 150 nm. The data coverage of hygroscopic state of mixing in the size range from $dp_{ve} = 150$ to 350 nm is poor. The reason for this is described in Section 2.3. There was no instrument available that gives the hygroscopic state of mixing in the size range $dp_{ve} > 350$ nm.

- In analogy to the DMPS, the HDMPS data have to be corrected for multiple charged particles. Therefore, information about the PNSD at 30%, 55%, 75% and 90% RH in the APS size range is required.

- The HDMPS measures the humidified PNSD and thus in combination with the DMPS they measured an average GF_{ve} at 30%, 55%, 75% and 90% RH, whereas the HAPS was operated at one RH of 85%. The problem to combine both to one humidified PNSD at the same RH has to be solved.

A new methodical approach is used here to derive RH-dependent hygroscopic growth factors and number fractions for a large size range including coarse mode particles. Therefore, this approach is described in detail here. In this manner, we perform a comparison of independent measurement techniques for the determination of the average volume equivalent hygroscopic growth factor. The comparison was performed in the size range, where both instruments overlap.

The following sections also explain how the problems expressed as bullet points above will be addressed.

2.5.1. Applying 'summation method' to calculate the average aerodynamic GF from HAPS and APS data. In a first step, measured HAPS data were corrected with the correction function shown in Fig. 4(b). A statistical model called 'summation method' (Birmili et al., 2009) was used to derive the average aerodynamic GF from HAPS and APS data. A short description of the 'summation method' is given in the following.

The number concentrations of the humidified and dry PNSD were summed bin-wise starting at the upper or lower end of the PNSDs. The obtained cumulative PNSDs were divided into logarithmically equidistant steps of cumulative number concentrations, because the cumulative PNSDs cover multiple orders of magnitude. The log-equidistant steps of the cumulative number concentrations of the dry and wet cumulative PNSD are iden-

tical. Finally, for each log-equidistant step of the cumulative number concentration, a discrete dry and wet particle diameter was attributed. The ratio of the wet to the dry particle diameter defines the average hygroscopic growth factor. Applying this procedure for each log-equidistant level, one obtains the average hygroscopic growth factor as a quasi-continuous function of the dry particle size.

For the HAPS and APS data, the number concentrations were summed bin-wise starting at the upper end of the PNSDs, ranging from 835 nm to 10 μm in aerodynamic diameter. Finally, the average aerodynamic growth factor was obtained as a quasi-continuous function of the dry particle diameter.

2.5.2. Extrapolation of GF_{ve} from HTDMA to the volume equivalent sizes > 350 nm and GF_{ve} parametrization. To address the problems stated in bullet points 1 and 2 (time-dependent hygroscopic state of mixing in the size range from 150 nm to 10 μm and conversion from aerodynamic to volume equivalent growth factor), the hygroscopic growth factors in the size range from 350 nm to 10 μm are required.

In the following paragraph, it was checked to extrapolate measured volume equivalent GFs at $dp_{ve} = 350$ nm to the size range from $dp_{ve} = 350$ nm to 10 μm. Figure 6 shows a box plot of the hygroscopic growth factors of the nearly hydrophobic and hygroscopic particles for the entire period. Hygroscopic growth factors from literature for sea-salt during ACE-Asia (Massling et al., 2007), and for more hygroscopic particles during ARI-ADNE at Crete (Stock et al., 2011) are added. The GFs during ACE-Asia were measured at 90% RH and were recalculated to 85% RH for comparison. In addition, reported GFs for mineral dust measured during SAMUM-1 in southern Morocco (Kaaden et al., 2009) are plotted into the graph. The literature values lie within the 10th and 90th percentile of the HTDMA growth factors measured at $dp_{ve} = 350$ nm. In this size range ($dp_{ve} > 350$nm), we assume sea-salt and mineral dust particles were the major compounds as supported by the mineralogical composition (cf. Fig. 9). There is no chemical explanation to observe internal mixtures of these components resulting in hygroscopic growth factors in between. Therefore, the time series of the HTDMA derived volume equivalent GFs at 350 nm was used to describe the volume equivalent GFs in the size range from $dp_{ve} = 350$ nm to 10 μm. Finally, the volume equivalent GFs were interpolated to the size bins of the discrete dry PNSD and then parameterized according to RH, using the single hygroscopicity parameter κ introduced in Petters and Kreidenweis (2007). This parameterization is based on modified Köhler theory, called κ-Köhler theory.

2.5.3. Calculation of number fractions in the APS size range. In the following, problems stated in Section 2.5 and bullet points 1 and 2 (time-dependent hygroscopic state of mixing in the size range from 150 nm to 10 μm and conversion from aerodynamic to volume equivalent hygroscopic growth factor) will be further addressed.
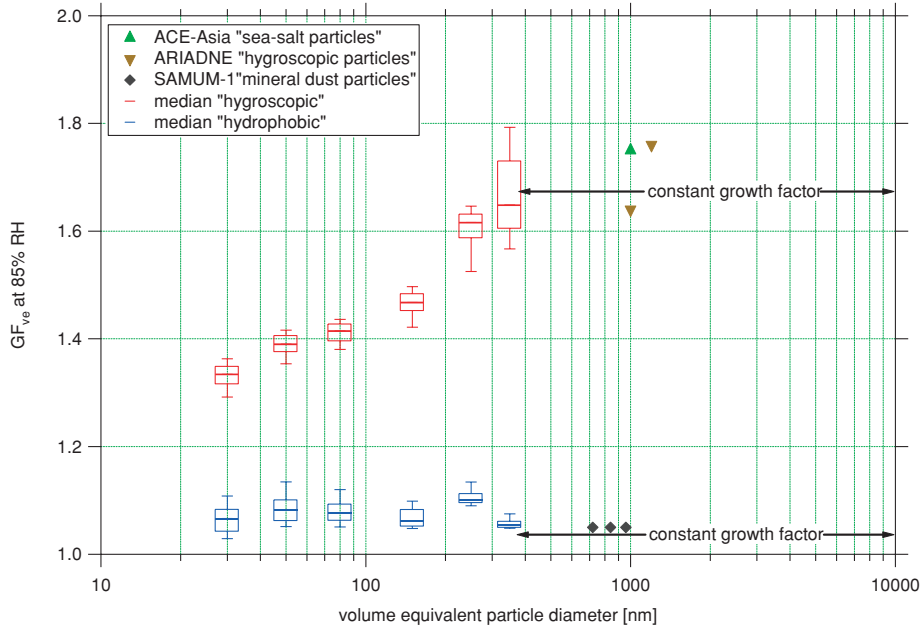
Fig. 6. Box plot of volume equivalent hygroscopic growth factors for the nearly hydrophobic and hygroscopic particles at 85% RH measured by the HTDMA. The whiskers represent the 10th and 90th percentile of the data. Hygroscopic growth factors for mineral dust (black markers), hygroscopic particles at the Mediterranean Sea (brown markers) and for sea-salt (green marker) are added.

The average volume equivalent hygroscopic growth factor is defined (e.g. Meier et al., 2009) as

$$\overline{GF_{ve}}^3 = \sum_i nf_i \cdot GF_{ve,i}^3, \tag{5}$$

where $GF_{ve,i}$ and nf_i are the hygroscopic growth factors and corresponding number fractions of the hygroscopic and nearly hydrophobic particles, respectively. Rearrangement of eq. (5) and using the expression $nf_{hyd} = 1 - nf_{hyg}$, the hygroscopic number fraction can be written as

$$nf_{hyg} = \frac{\overline{GF_{ve}}^3 - GF_{ve,hyd}^3}{GF_{ve,hyg}^3 - GF_{ve,hyd}^3}. \tag{6}$$

The following formula is derived to convert the volume equivalent growth factors into aerodynamic growth factors. In analogy to eq. (4), the aerodynamic growth factor is defined as

$$GF_a(RH) = \frac{dp_a(RH)}{dp_a(dry)}. \tag{7}$$

Combining eqs (2), (4) and (7), and introducing the solution droplet density $\rho(RH)$ and the dynamic shape factor $\chi(RH)$, this leads to the following expression:

$$GF_a(RH) = GF_{ve}(RH) \cdot \sqrt{\frac{\rho(RH) \cdot \chi}{\rho_p \cdot \chi(RH)}}. \tag{8}$$

Obviously, after humidification a hygroscopic particle is spherical and therefore $\chi(RH = 85\%) = 1.0$ $\rho(RH)$ is calculated using a volume mixing rule (e.g. Leinert and Wiedensohler,

2008):

$$\rho(RH) = \frac{1}{GF_{ve}(RH)^3} \cdot \rho_p + \left(1 - \frac{1}{GF_{ve}(RH)^3}\right) \cdot \rho_w, \tag{9}$$

where ρ_w is the density of water.

Finally, combining eqs (8) and (9) leads to a formula to calculate aerodynamic hygroscopic growth factors from the volume equivalent GFs in the APS size range:

$$GF_a(RH) = \sqrt{\frac{\chi + \frac{\chi \cdot \rho_w}{\rho_p}\left(GF_{ve}(RH)^3 - 1\right)}{\chi(RH) \cdot GF_{ve}(RH)}}. \tag{10}$$

For example, assuming $\chi = 1.08$, $\chi(RH = 85\%) = 1.0$, $\rho_p = 2160$ kg m^{-3} and $GF_{ve}(RH = 85\%) = 1.8$, the aerodynamic growth factor $GF_a(RH = 85\%)$ is 1.394.

Now, all informations are available to calculate number fractions of hygroscopic and nearly hydrophobic particles in the APS size range by replacing in eq. (6) the respective GF_{ve} to GF_a as

$$nf_{hyg} = \frac{\overline{GF_a}^3 - GF_{a,hyd}^3}{GF_{a,hyg}^3 - GF_{a,hyd}^3}. \tag{11}$$

In eq. (11), $\overline{GF_a}$ is the measured average aerodynamic growth factor and $GF_{a,hyd}$ and $GF_{a,hyg}$ are the calculated aerodynamic growth factors (nearly hydrophobic and hygroscopic particles) from eq. (10).

2.5.4. Calculation of PNSDs at 30%, 55%, 75% and 90% RH in the APS size range and merging with humidified PNSDs from HDMPS. This section addresses problems stated in Section 2.5 and bullet points 3 and 4 (HDMPS/DMPS measured an average

GF at 30%, 55%, 75% and 90% RH, whereas the HAPS was operated at 85% RH and HDMPS data had to be corrected for multiple charged particles).

By using the hygroscopicity parameter κ, the volume equivalent hygroscopic growth factors were calculated at 30%, 55%, 75% and 90% RH for the APS size range. Afterwards, the average volume equivalent GF was calculated at the four RHs applying eq. (5). Finally, the PNSD at 30%, 55%, 75% and 90% RH in the APS size range was calculated, by multiplying the dry PNSD bin-wise with the respective RH-dependent average volume equivalent GF.

The HDMPS raw data were classified into different RH intervals of RH = 30 ± 3%, 55 ± 3%, 75 ± 3% and 90 ± 3%. Secondly, the multiple charge correction (APS size range particles) was applied using the PNSD at 30%, 55%, 75% and 90% RH in the APS size range. Thirdly, the HDMPS data were inverted using the regular inversion algorithm (Stratmann and Wiedensohler, 1996).

Fourthly, the humidified PNSDs in the HDMPS size range were corrected using the RH-dependent correction functions shown in Fig. 4(a). Finally, the humidified PNSDs at 30%, 55%, 75% and 90% RH in the HDMPS and in the HAPS size range were merged to final PNSDs ranging from 26 nm < dp_{ve} < 10 μm.

2.5.5. Applying the 'summation method' to calculate average volume equivalent hygroscopic growth factors in the size range from 26 nm < dp_{ve} < 10 μm. First, the 'summation method' in the size range from 26 nm < dp_{ve} < 10 μm was applied to obtain the average volume equivalent GF of a certain particle size. At this stage, we review two different methods to measure average volume equivalent GF. The first method to derive average volume equivalent GFs is to use the HTDMA, whereas the second method is based on a statistical evaluation (summation method) of the HDMPS data.

The HTDMA-derived growth factor probability density function (GF-PDF) at RH = 85% was recalculated to 90% RH using eq. (3) from Gysel et al. (2009). Afterwards, the normalized GF-PDF was integrated over the full GF range to yield an average GF_{ve} for the selected particle size. Figure 7 shows an intercomparison study for average volume equivalent GFs of the six selected initial diameters by the HTDMA. Generally, for dp_{ve} = 150, 250 and 350 nm the values lie on the 1:1 line, whereas the values for dp_{ve} = 30, 50 and 80 nm of the HDMPS method underestimate the HTDMA average volume equivalent GFs. Considering the smallest three selected diameters (dp_{ve} = 30, 50 and 80 nm), the deviation from the 1:1 line is largest for the smallest particles. This behaviour is also seen in Fig. 7 in Meier et al. (2009), and is an artefact of the 'summation method'. The statistical evaluation of the HDMPS data claims conservation for the total number concentration when the particles are humidified from the dry to the wet state. Hence, in most of the time this demand is however not fulfilled. For this case, a maximum deviation of the total particle number concen-
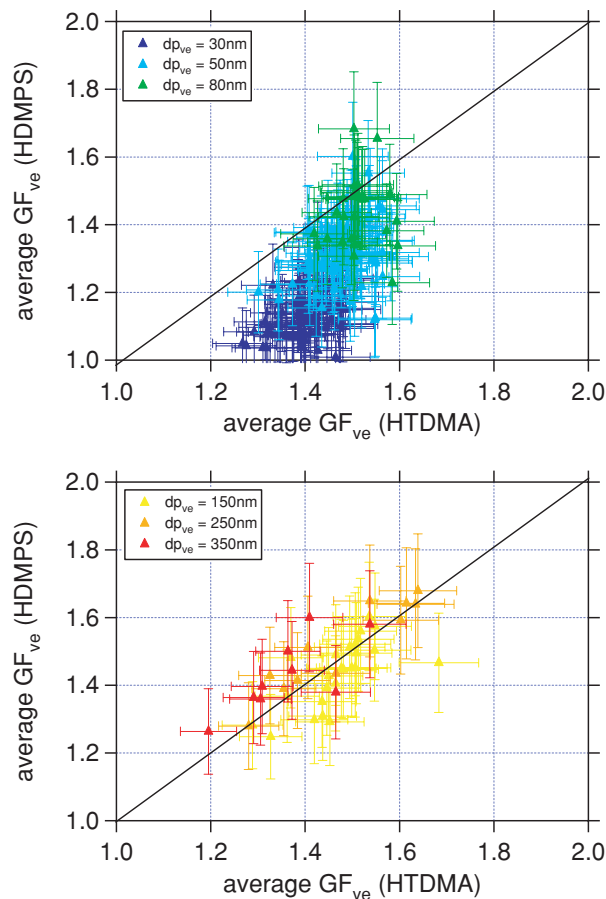

Fig. 7. Intercomparison of average volume equivalent hygroscopic growth factors from HTDMA and HDMPS at RH = 90% for six dry diameters. Error bars for average volume equivalent GFs from HDMPS (10%) and HTDMA (5%) are added.

tration of 15% was allowed, because it considers the counting error of both APS. The result is that the 'summation method' derived average volume equivalent GFs are underestimated for the smallest diameters, when the PNSD is accumulated from the upper end.

2.5.6. Calculation of number fractions in the intermediate size range from 150 nm < dp_{ve} < 570 nm. This section will address the problem discussed in bullet point 2 of Section 2.5 (time-dependent hygroscopic state of mixing in the size range from 150 nm to 10 μm).

Because of the exclusion of biased HTDMA-derived number fractions especially for dp_{ve} = 150, 250 and 350 nm, quasi-continuous number fractions from the HTDMA are only available in the size range from 30 nm < dp_{ve} < 80 nm. Quasi-continuous number fractions in the size range dp_{ve} > 570 nm are delivered by calculations based on HAPS data (cf. Section 2.5.3). The number fractions in the intermediate size range were calculated according to eq. (6), by using the measured size

resolved average volume equivalent GFs from the HDMPS and the corresponding volume equivalent GFs at the same RHs.

2.5.7. Error discussion of growth factors, derived κ values and number fractions. The uncertainty of the hygroscopic growth factors depends mainly on the RH uncertainty within the HTDMA system. At 90% RH, the manufacturers give absolute uncertainties of 1% for the humidity sensors, and 0.5% for the dew point mirror sensor, respectively. Considering the uncertainty when the GF_{ve} was corrected to the set point RH, as shown in Gysel et al. (2009) in their Fig. 6, an overall uncertainty of 5% for the volume equivalent GFs as well as for κ values was estimated. This uncertainty is in agreement with reported values from HTDMA measurements (Massling et al., 2007). The uncertainty of the number fractions for $dp_{ve} < 150$ nm results from the HTDMA, whereas the uncertainty for $dp_{ve} > 150$ nm results from average volume equivalent GFs as well as from uncertainties of volume equivalent GFs. To estimate the uncertainty of the number fractions for $dp_{ve} > 150$ nm, the uncertainty of the average volume equivalent GF needs to be quantified.

The uncertainty of the average volume equivalent GF is composed of uncertainties in RH and deviations in the PNSD. Here, deviations of up to 15% in the total particle concentration of the dry and humidified PNSD involve the largest source of error. Because the average deviations of the total particle number concentrations are however smaller than 15%, an uncertainty of the average (volume equivalent and aerodynamic) GF of 10% for HDMPS- and HAPS-derived data were estimated.

Applying error propagation, the uncertainty for the number fractions in the size range $dp_{ve} > 150$ nm is about 24%.

2.6. Single particle analysis

Aerosol sampling for single particle analysis was carried out with a miniature cascade impactor on top of the container on a three-dimensional wind vane that provides isoaxial sampling of particles up to 30 μm in diameter. Impaction samples of aerosol particles were taken up to two times each day for 5–180 s. The samples were analysed by scanning electron microscopy of single particles. A detailed description of sampling and analytical techniques is given in Kandler et al. (2011b). The analysed sample dates for this work were: DOY 18.65, 19.76, 25.63, 28.39, 28.71, 35.63, 35.76, 36.58, 36.76, 37.56, 38.43, 39.43 and 40.42 local time (LT). Based on the chemical composition derived from X-ray count rates, particles were classified into 25 different groups. Then, the particles were classified into logarithmically equidistant size classes according to their projected area diameter.

2.7. Particle mass concentration

Particle mass concentrations of PM_{10} and $PM_{2.5}$ equivalent were measured daily with a filter sampler on top of the measurement container in a height of about 4 m above ground.

The particle sizes sampled on the filter are determined by a pre-impactor. Total suspended (TSP) mass concentrations were measured daily with a high volume sampler on top of the container (same height as filter sampler) on a wind vane to achieve isoaxial sampling. Further details are given in Kandler et al. (2011a). The $PM_{2.5}$, PM_{10} and TSP mass concentrations were determined by gravimetry of the filter samples, the flow rate through the filter sampler and the measurement duration of the filter. The weighing with a microbalance was performed at a constant RH of about 55% and thus, the mass concentrations were derived at the same RH.

3. Results and discussion

3.1. Parametrized particle number size distributions

A statistical analysis of the dry PNSD from the entire measurement period is shown in Fig. 8. However, the position of fitted lognormal size distribution shown in the plot was not arbitrarily chosen.

Two fine particle modes (blue solid lines in Fig. 8) represent the typical bimodal submicrometre marine PNSD composed of an Aitken and an accumulation mode.

In a review paper on marine aerosols (Fitzgerald, 1991), the geometric mean diameters of the bimodal marine PNSD are reported in the range of $d_g = 40$–60 nm and $d_g = 180$–300 nm, respectively. The fine fraction of the marine (background) aerosol, typically in the size range $dp_{ve} < 600$ nm, is explained primarily as non–sea-salt sulphate (NSS), formed by gas-to-particle conversion of the oxidation products of organosulphur gases (primarily DMS[1]) released by the ocean (Fitzgerald, 1991). The typical marine double peak characteristic is caused through cloud processing of non–precipitating clouds (Hoppel et al., 1990). In clouds, trace gases such as SO_2 are absorbed by cloud droplets and are converted to particulate matter such as sulphates (Fitzgerald, 1991). The aerosol particles remaining after the evaporation are larger than the original ones. The average mineralogical composition derived from the single particle analysis is shown in Fig. 9. It shows that a large fraction of sulphate particles in the fine mode are ammonium sulphate, which is in accordance to former studies (e.g. Mészáros and Vissy, 1974; Gras and Ayers, 1983). Therefore, a dry particle density of $\rho_p = 1700$ kg m^{-3} for the fine mode was assumed.

Considering the argumentation in Section 2.5.2, the coarse particle modes (green solid lines in Fig. 8) represent the external mixture of sea-salt and Saharan mineral dust particles. Gras and Ayers (1983) point out that in the clean marine environment essentially all particles larger than $dp_{ve} = 600$ nm consist of sea-salt. As seen in Fig. 9 the components of mineral dust, for example silicates and quartz occur nearly in the same size range like sea-salt particles, which in turn consist of sodium
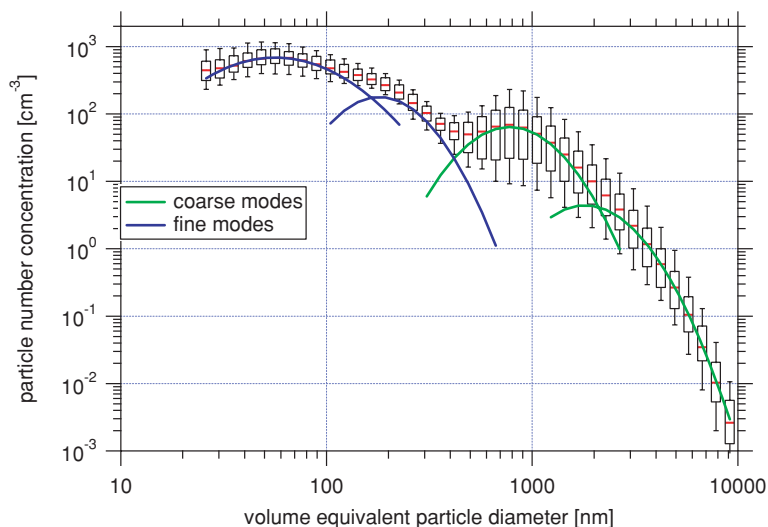
---

[1]dimethyl sulfide

Fig. 8. Box plot of the dry PNSD for the entire measurement period, as well as fitted lognormal size distributions. The whiskers represent the 10th and 90th percentile of the data.
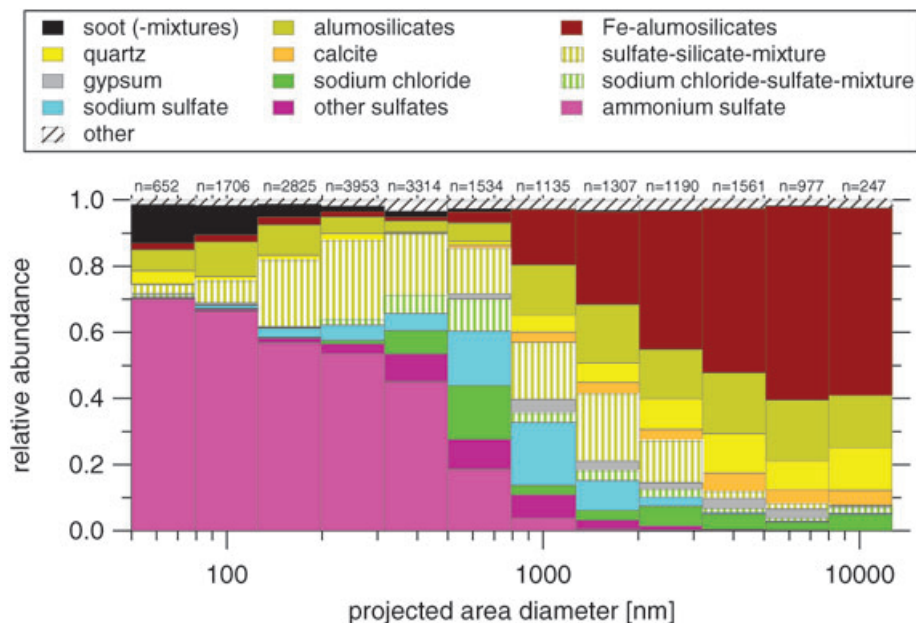

Fig. 9. Average mineralogical composition for 12 components, derived from single particle analysis. Components having a relative abundance <1% were grouped into 'other'. The total number of analysed particles '*n*' is given for each size class.

chloride and sodium sulphate. For comparison, Table 2 shows the lognormal size distribution parameters for the dry PNSD (Kaaden et al., 2009; Schladitz et al., 2009) during SAMUM-1, which was conducted near a Saharan dust source region. The geometric mean diameter in SAMUM-1 agrees with the fitted (first) coarse mode d_g shown in Fig. 8. Hence, the first coarse mode can be directly attributed to the sea-salt and mineral dust particles. The second coarse mode was achieved for the sake of conservation of particle number, surface and volume concentration. It is most likely that the second coarse mode contributes to the first coarse mode and has therefore the same chemical composition.

Table 2 summarizes the arithmetic mean value and single standard deviation for the lognormal size distribution parameters. Generally, within each particle mode, the variation of N is larger than the variation of d_g and σ_g, respectively. The largest variations of N show the coarse modes, followed by the accumulation and Aitken modes. Typical total particle number concentrations for the Aitken and accumulation modes over central regions of the Atlantic are $600 \, \text{cm}^{-3}$ on average (Junge and Jaenicke, 1971) and $50–100 \, \text{cm}^{-3}$ (O'Dowd et al., 1997), respectively. These values agree with the values found in this study of $541 \pm 247 \, \text{cm}^{-3}$ for the Aitken mode and $84 \pm 42 \, \text{cm}^{-3}$ for the accumulation mode.

Table 2. Parameters of the dry PNSD during SAMUM-1 conducted in southern Morocco (Kaaden et al., 2009; Schladitz et al., 2009) and arithmetic mean value ± single standard deviation for the parameters of the lognormal size distributions during SAMUM-2.

	Mode name	N (cm^{-3})	d_g (nm)	σ_g
SAMUM-1	Coarse	70	630	1.75
	Accumulation	450	95	1.8
	Aitken	180	32	1.5
SAMUM-2	Coarse 2	3.9 ± 5.4	1790 ± 328	1.54 ± 0.07
	Coarse 1	39.4 ± 37	780 ± 49	1.52 ± 0.05
	Accumulation	84 ± 42.5	177 ± 17.5	1.5 ± 0.07
	Aitken	541 ± 247	53 ± 11	1.9 ± 0.11

The large variation of N in the coarse mode is exemplified in the following:

Some investigations (e.g. Fitzgerald, 1991; O'Dowd and Smith, 1993; O'Dowd et al., 1997) found a connection of the particle number concentration of the marine aerosol—in particular for the sea-salt fraction—and the actual wind speed over the ocean. In our study, the sea-salt variation in N is superimposed by the contribution of Saharan mineral dust particles in the coarse mode. Hence, the later section confirms that the variation of the amount of mineral dust is much larger than the variation of the sea-salt content in the coarse mode.

3.2. Hygroscopicity parameter κ and number fractions

A statistical analysis of the hygroscopicity parameter κ for the entire measurement period is shown in Fig. 10. For the hygroscopic particles, κ is nearly constant in the size range $dp_{ve} <$ 100 nm with a median around 0.35 and increases to $\kappa = 0.65$ in the subsequent size range from 100 nm $< dp_{ve} <$ 350 nm. In the size range $dp_{ve} >$ 350 nm, κ was set constant as discussed above. For the nearly hydrophobic particles, κ varies between 0

and 0.1 in the size range up to $dp_{ve} <$ 250 nm. For larger particles ($dp_{ve} >$ 250 nm), κ decreases towards 0.

The variation within κ is largest for the hygroscopic particles in the size range $dp_{ve} >$ 250 nm. The size dependency of the hygroscopicity parameter κ can be explained by hygroscopic materials from the mineralogical composition. From the mineralogical composition (Fig. 9) it is obvious that different species of hygroscopic materials are present: sodium chloride, sodium chloride–sulphate mixtures, sodium sulphate, ammonium sulphate and other undetermined and mixed (sodium–potassium–calcium) sulphates. The size segregated average fractions of the three major inorganic salts—sodium chloride, sodium sulphate and ammonium sulphate—are shown in Fig. 11. Note that Figs. 10 and 11 are based on different particle diameter definitions.

It is seen from Fig. 11 that in the size range $dp <$ 100 nm ammonium sulphate is the predominant hygroscopic component. In the following, the hygroscopicity parameter κ is compared with literature values. In Petters and Kreidenweis (2007), κ parameters of pure inorganic salts are given, which were derived from hygroscopic growth factor and CCN measurements. For reasons of improved comparison, the hygroscopic growth factor derived κ parameter was chosen. The measured κ values of this investigation are on the lower scale of the reported values for pure ammonium sulphate that ranges from 0.33 to 0.72. A possible reason is the internal mixture with one or more hydrophobic substances. This assumption was supported by Kandler et al. (2011b), who found ammonium sulphate particles internally mixed with soot, as well as hints of a possibly organic coating.

In the size range from 100 nm $< dp_{ve} <$ 300 nm, the increase of the hygroscopicity parameter κ with particle size is caused by the large fraction of sulphate within the particle, which was produced through cloud processing. The subsequent increase of κ with particle size correlates with the increasing fraction of
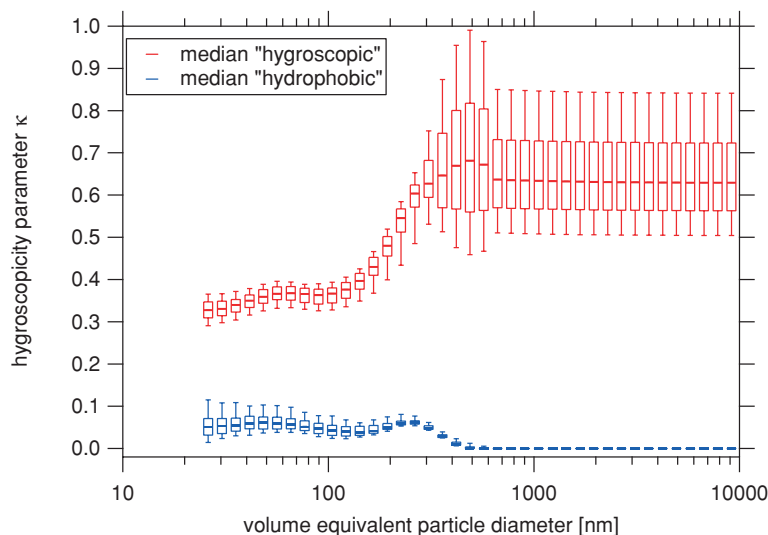

Fig. 10. Box plot of the hygroscopicity parameter κ for hygroscopic and nearly hydrophobic particles for the entire measurement period. The whiskers represent the 10th and 90th percentile of the data.
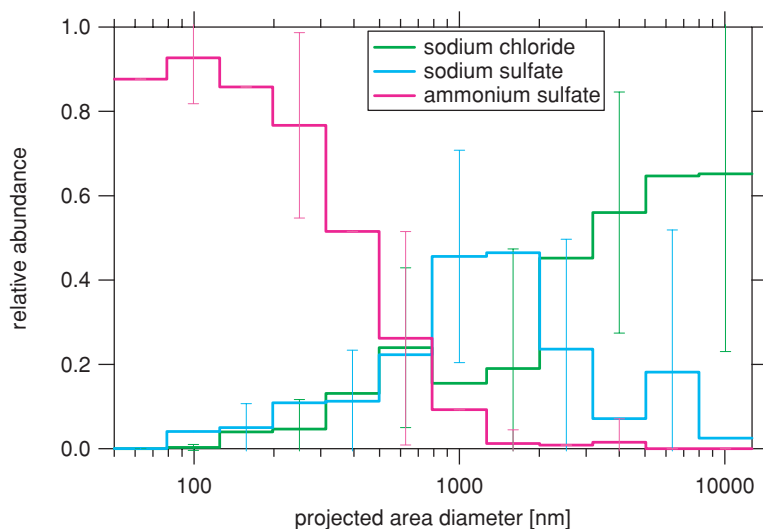
more hygroscopic materials, for example sodium chloride and sodium sulphate.

The reported κ values for sodium chloride and sodium sulphate are 0.91–1.33 and 0.68, respectively (Petters and Kreidenweis, 2007). Again, the measured values are on the lower scale of the literature values. Nevertheless, Niedermeier et al. (2008) report slightly lower hygroscopic growth of sea-salt particles compared to pure sodium chloride particles. Furthermore, organic compounds in the uppermost thin layers of the sea-water reduce the hygroscopic growth compared to pure sodium chloride. The larger variation of κ in the size range $dp_{ve} > 250$ nm is caused by the variability, represented by the single standard deviation of the sodium sulphate and sodium chloride fraction in Fig. 11.

Figure 12 illustrates the number fraction of nearly hydrophobic particles as a contour plot. As stated earlier, the difference to unity equals the number fraction of hygroscopic particles. In general, the number fraction of nearly hydrophobic particles is larger in the coarse particle mode than in the fine particle mode. The highest (reddish) values occur for mineral dust particles in the coarse particle mode. For this mode, the number fraction of mineral dust is still variable, with maxima close to 1, between DOY 24.5–26.5 LT and DOY 28–34 LT. The lowest values with minima of ∼0.3 occur in the last period from DOY 34 LT. From Fig. 12, the influence of dust particles was observed down to $dp_{ve} = 300$ nm, which agrees with the smallest observed dust particles by Kaaden et al. (2009) during SAMUM-1.

In contrast to the larger particles, Fig. 9 reveals that soot and probably some silicate particles are the main hydrophobic component in the fine particle mode. Assuming that soot particles were completely externally mixed, the hydrophobic mass concentration derived from the number fraction of nearly hydrophobic particles in the fine particle mode and the mass concentration of soot, derived from RAMAN spectroscopy (Schladitz et al.,

2011), would be positively correlated. However, this is not the case. Cheng et al. (2006) point out that soot from long-range transport is more internally mixed. Kandler et al. (2011b) found some ammonium sulphate particles internally mixed with soot, as well as sulphate particles without soot and pure soot particles externally mixed. In addition, Massling et al. (2007) argued that the hydrophobic particles in the fine particle mode can be attributed to freshly emitted externally mixed soot particles. Hence, from the argumentation above it is concluded that soot particles at Cape Verde were internally as well as externally mixed and the temporal variation of the number fraction of nearly hydrophobic particles in the fine mode was caused by changes in the mixing ratio of externally and internally mixed soot particles.

4. Verification of results

This section verifies the findings in Section 3 and confirms the assumptions have been made in this work. For this case, a mass closure at ambient conditions was performed.

To carry out a mass closure at ambient conditions, ambient temperature, pressure and RH, has to be considered. Temperature and pressure during the measurement of the dry PNSD and during the measured PM_{10} and TSP mass concentrations at ambient conditions were nearly the same. However, the PM_{10} and TSP mass concentrations were determined at about 55% RH, which deviates from the actual measured ambient RH at the site.

First, the dry PNSD was transformed to ambient conditions. For this case, the size-dependent particle transmission efficiency from outside to the instruments (Schladitz et al., 2011) was applied. Afterwards, each bin of the dry PNSD was multiplied with the time- and size-dependent number fraction of hygroscopic and nearly hydrophobic particles. Simultaneously, the dry diameters of the hygroscopic and nearly hydrophobic particles were multiplied bin-wise with the volume equivalent hygroscopic growth
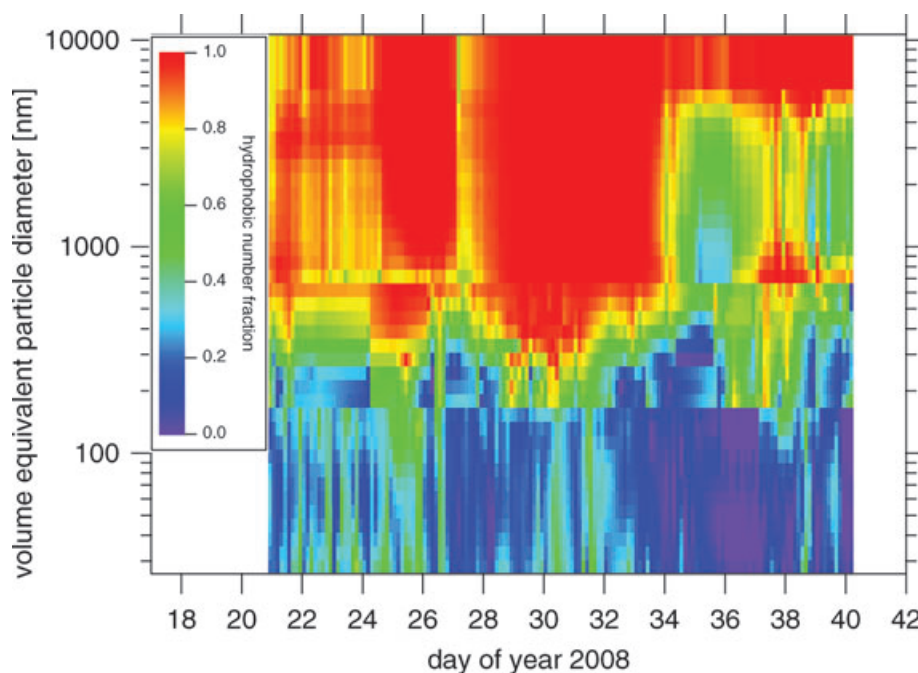
Fig. 12. Contour plot of the number fraction of nearly hydrophobic particles for the entire measurement period. As seen by some discontinuities, this plot was put together based on data from HTDMA ($dp_{ve} < 150$ nm), HDMPS (150 nm $< dp_{ve} <$ 570 nm) and HAPS ($dp_{ve} > 570$ nm).
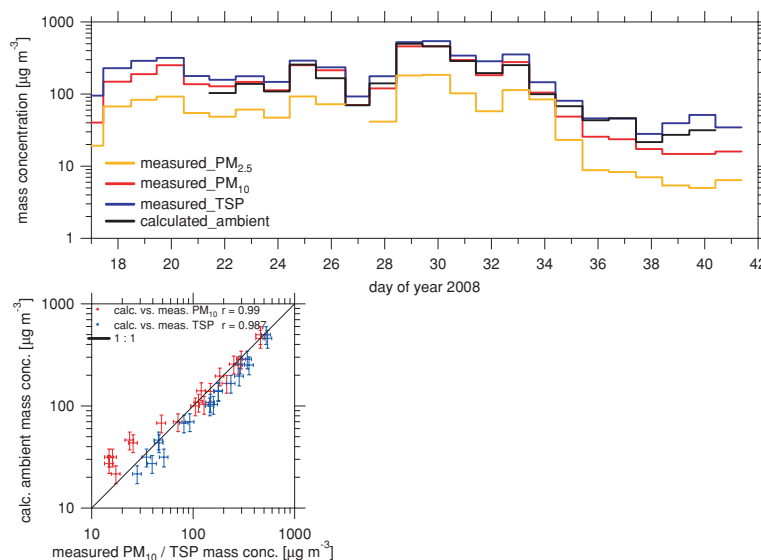

Fig. 13. Mass closure at ambient conditions performed at 55% RH. The upper panel shows a time series of measured PM$_{2.5}$, PM$_{10}$ and TSP as well as calculated mass concentration. The lower panel shows a scatter plot of calculated versus measured PM$_{10}$ and TSP mass concentration, respectively. The error of the calculated mass concentration was estimated to as 20% regarding uncertainties in quantifying the transmission efficiency of the dry PNSD.

factors at RH = 55%, which were in turn determined by the time- and size-dependent κ parameters. To ensure conservation of the total particle number concentration, the number concentrations of the size bins in $dN/\mathrm{dlog}dp_{ve}$ were modified according to the change of the size interval width. The solution droplet density $\rho(\mathrm{RH} = 55\%)$ was calculated bin-wise using eq. (9) and the time- and size-dependent volume equivalent hygroscopic growth factors at RH = 55%. The respective dry particle density ρ_p for each mode (fine and coarse) and particle composition

(sea-salt and Saharan mineral dust) is given above in Sections 2.2 and 3.1.

The upper panel of Fig. 13 shows the time series of measured PM$_{2.5}$, PM$_{10}$ and TSP as well as calculated ambient mass concentrations (averages according to the sampling periods) at about RH = 55% based on the procedure described earlier. Measured TSP mass concentrations range from 28 to 542 μg m^{-3}, whereas the measured PM$_{10}$ to TSP mass concentration ratio is between 28% and 91% with an arithmetic mean of 68%. The

lowest PM_{10} to TSP mass concentration ratio occurs in the last period starting DOY 34, with the lowest mass concentrations during the entire measurement period. The time series of the $PM_{2.5}$ mass concentration shows a similar trend when comparing with the PM_{10} and TSP mass concentration. Here the coarse mode particles appear with a much larger mass fraction within $PM_{2.5}$ than in the fine mode. The lower panel in Fig. 13 shows a scatter plot of calculated ambient mass concentration at RH = 55% versus measured PM_{10} and TSP mass concentration. In general, the calculations and the measurements correlate perfectly ($r = 0.99$) and lie close to the 1:1 line indicating the successful recalculation of particle mass concentrations by particle number based measurements. To be more specific, for high-measured mass concentrations before DOY 34 LT, the calculated ambient and measured PM_{10} mass concentrations lie directly on the 1:1 line. In contrast to that, for lower mass concentrations (starting DOY 34 LT), the calculated ambient mass concentration is closer to the measured TSP than to the PM_{10} values. This finding gives a hint that the mass increase due to hygroscopic growth of large sea-salt particles significantly exceeds the measured PM_{10} value as the calculations are sensitive to these large particles and their hygroscopic behavior. In summary, the ratio of calculated ambient mass concentration to measured TSP mass concentration is between 61% and 101% with an arithmetic mean value of 79%. Hence, taking the illustrated error bars into account, the mass closure was successful.

5. Summary and conclusion

This study presents comprehensive data of parametrized particle number size distribution as well as hygroscopic growth factors in the size range from $dp_{ve} = 26$ nm to 10 μm for marine and Saharan mineral dust aerosols. Dry particle number size distributions show typical Aitken and accumulation modes with geometric mean diameters of 53 and 177 nm on average. Sea-salt and mineral dust particles appeared in the coarse mode with an geometric mean diameter of 780 nm. This value agrees with the measured geometric mean diameter of freshly emitted Saharan dust particles during SAMUM-1. In contrast to the fine modes, the particle number concentration of the coarse mode is highly variable and depends on the transport of mineral dust from the Saharan desert.

A new methodical approach was presented to derive size segregated, time-dependent volume equivalent hygroscopic growth factors and corresponding number fractions in a size range from $dp_{ve} = 26$ nm to 10 μm by instruments operated at different relative humidities (HDMPS, HAPS and HTDMA) and size spectrometers (DMPS, APS) operated at dry conditions. The results from the HTDMA revealed an external mixture of nearly hydrophobic ($GF_{ve} < 1.2$) and hygroscopic ($GF_{ve} > 1.2$) particles in the size range $dp_{ve} < 350$ nm. For particles larger than $dp_{ve} > 350$ nm, the number fractions are based on calculations.

However, in contrast to volume equivalent hygroscopic growth factors, the number fractions show a high variability, especially for the coarse mode particles. The externally mixed nearly hydrophobic particle fraction belongs to Saharan mineral dust particles, whereas the hygroscopic fraction is linked to sea-salt particles. Average volume equivalent hygroscopic growth factors were compared with two independent measurement methods at $dp_{ve} = 30, 50, 80, 150, 250$ and 350 nm. In a scatter plot, the values for $dp_{ve} = 150, 250$ and 350 nm lie on the 1:1 line, whereas the values for $dp_{ve} = 30, 50$ and 80 nm of the HDMPS method underestimate the HTDMA average volume equivalent GFs. The underestimation can be explained by an artefact of the HDMPS method to derive average volume equivalent GFs.

From measured volume equivalent hygroscopic growth factors by the HTDMA, the hygroscopicity parameter κ was calculated. For hygroscopic particles, κ is nearly constant in the size range $dp_{ve} < 100$ nm with a median around 0.35 and increases to $\kappa = 0.65$ in the size range from 100 nm $< dp_{ve} <$ 350 nm. For larger particles, the time-dependent κ parameters at $dp_{ve} = 350$ nm were used. κ is on the lower scale of reported κ values for ammonium sulphate, which was found to be the main hygroscopic component in the fine mode. However, results from mineralogical single particle analysis specify ammonium sulphate particles to be internally mixed with soot, as well as hints of organic coating, explaining this lower value for the hygroscopicity parameter. For the nearly hydrophobic particles, κ varies between 0 and 0.1 in the size range up to $dp_{ve} = 250$ nm. For larger particles, κ decreases towards 0. It is assumed that nearly hydrophobic particles in the fine mode consist of externally mixed soot particles. The method to derive the presented κ values implies that the hygroscopic growth factors are only valid in a RH range from 0% to 90% and for particles being in metastable equilibrium with the surrounding moist air.

A mass closure at ambient conditions was carried out using gravimetric determined mass concentrations of PM_{10} and TSP at 55% RH and calculated particle mass concentrations based on particle number based measurements. In a scatter plot, the measured and calculated values lie close to the 1:1 line and show correlations of about $r = 0.99$ and verifies the findings of this study. The calculated particle mass concentration agreed better with TSP than with PM_{10}, which demonstrates the important role of hygroscopic growth of large hygroscopic sea-salt particles for this mass closure experiment.

This work delivers an extensive study on hygroscopic growth of mixed marine and Saharan mineral dust aerosols, which are the largest particle sources worldwide. The parametrizations of this study can be used to include hygroscopic particle growth in GCMs. With this additional information on particle behavior under ambient conditions, the direct radiative forcing of particles can be calculated more realistically. The results of this work were already used in the second part of this paper, to investigate the influence of humidity on important aerosol optical properties.

6. Acknowledgments

References

Ansmann, A., Petzold, A., Kandler, K., Tegen, I., Wendisch, M. and co-authors. 2011. Saharan mineral dust experiments SAMUM-1 and SAMUM-2: what have we learned? *Tellus* **63B**, this issue.

Berg, O. H., Swietlicki, E. and Krejci, R. 1998. Hygroscopic growth of aerosol particles in the marine boundary layer over the Pacific and Southern Oceans during the First Aerosol Characterization Experiment (ACE 1). *J. Geophys. Res.* **103**, 16535–16545.

Birmili, W. 1998. *Production of New Ultrafine Particles in Continental Air Masses*. PhD Thesis, University of Leipzig, Germany.

Birmili, W., Stratmann, F. and Wiedensohler, A. 1999. Design of a DMA-based size spectrometer for a large particle size range and stable operation. *J. Aerosol Sci.* **30**, 549–553.

Birmili, W., Schepanski, K., Ansmann, A., Spindler, G., Tegen, I. and co-authors .2008. A case of extreme particulate matter concentrations over Central Europe caused by dust emitted over the southern Ukraine. *Atmos. Chem. Phys.* **8**, 997–1016.

Birmili, W., Schwirn, K., Nowak, A., Petäjä, T., Joutsensaari, J. and co-authors. 2009. Measurements of humidified particle number size distributions in a Finnish boreal forest: derivation of hygroscopic particle growth factors. *Boreal Environ. Res.* **14**, 458–480.

Cheng, Y. F., Eichler, H., Wiedensohler, A., Heintzenberg, J., Zhang, Y. H. and co-authors. 2006. Mixing state of elemental carbon and non-light-absorbing aerosol components derived from in situ particle optical properties at Xinken in Pearl River Delta of China. *J. Geophys. Res.* **111**, D20204, doi:10.1029/2005JD006929.

Chiapello, I., Bergametti, G., Gomes, L., Chatenet, B., Dulac, F. and co-authors. 1995. An additional low layer transport of Sahelian and Saharan dust over the North-Eastern Tropical Atlantic. *Geophys. Res. Lett.* **22**, 3191–3194.

Chiapello, I., Bergametti, G., Chatenet, B., Bousquet, P., Dulac, F. and co-authors. 1997. Origins of African dust transported over the north-eastern tropical Atlantic. *J. Geophys. Res.* **102**, 13701–13709.

Covert, D. S., Charlson, R. J. and Ahlquist, N. C. 1972. A study of the relationship of chemical composition and humidity to light scattering by aerosols. *J. Appl. Meteor.* **11**, 968–976.

DeCarlo, P. F., Slowik, J. G., Worsnop, D. R., Davidovits, P. and Jimenez, J. L. 2004. Particle morphology and density characterization by combined mobility and aerodynamic diameter measurements. Part 1: theory. *Aerosol Sci. Technol.* **38**, 1185–1205.

Duplissy, J., Gysel, M., Sjogren, S., Meyer, N., Good, N. and co-authors. 2009. Intercomparison study of six HTDMAs: results and recommendations. *Atmos. Meas. Tech.* **2**, 363–378.

Engelstaedter, S., Tegen, I. and Washington, R. 2006. North African dust emissions and transport. *Earth-Sci. Rev.* **79**, 73–100.

Fitzgerald, J. W. 1991. Marine aerosols: a review. *Atmos. Environ.* **25**, 533–545.

Forster, P., Ramaswamy, V., Artaxo, P., Berntsen, T., Betts, R. and co-authors. 2007. Changes in atmospheric constituents and in radiative forcing. In: *Climate Change 2007: The Physical Science Basis. Contribution of Working Group I to the Fourth Assessment Report of the Intergovernmental Panel on Climate Change* (eds. Solomon, S., Qin, D., Manning, M., Chen, Z., Marquis, M., Averyt, K. B., Tignor, M. and Miller, H. L.). Cambridge University Press, Cambridge, UK and New York, USA.

Gras, J. L. and Ayers, G. P. 1983. Marine aerosol at Southern Mid-Latitudes. *J. Geophys. Res.* **88**, 10661–10666.

Gysel, M., Weingartner, E. and Baltensperger, U. 2002. Hygroscopicity of aerosol particles at low temperatures. 2. Theoretical and experimental hygroscopic properties of laboratory generated aerosols. *Environ. Sci. Technol.* **36**, 63–68.

Gysel, M., McFiggans, G. B. and Coe, H. 2009. Inversion of tandem differential mobility analyser (TDMA) measurements. *J. Aerosol Sci.* **40**, 134–151.

Hänel, G. 1976. The properties of atmospheric aerosol particles as functions of the relative humidity at thermodynamic equilibrium with the surrounding moist air. *Adv. Geophys.* **19**, 74–189.

Haywood, J. M., Francis, P. N., Glew, M. D. and Taylor, J. P. 2001. Optical properties and direct radiative effect of Saharan dust: a case study of two Saharan dust outbreaks using aircraft data. *J. Geophys. Res.* **106**, 18417–18430.

Hoppel, W. A., Fitzgerald, J. W., Frick, G. M., Larson, R. E. and Mack, E. J. 1990. Aerosol size distributions and optical properties found in the marine boundary layer over the Atlantic ocean. *J. Geophys. Res.* **95**, 3659–3686.

IPCC 2007. *Climate Change 2007: The Physical Science Basis. Contributions of Working Group I to the Fourth Assessment Report of the Intergovernmental Panel on Climate Change*. Cambridge University Press, Cambridge, UK and New York, USA.

Jokinen, V. and Mäkelä, J. M. 1997. Closed-loop arrangement with critical orifice for DMA sheath/excess flow system. *J. Aerosol Sci.* **28**, 643–648.

Junge, C. and Jaenicke, R. 1971. New results in background aerosols studies from the Atlantic expedition of the R.V. Meteor, Spring 1969. *J. Aerosol Sci.* **2**, 305–314.

Kaaden, N., Massling, A., Schladitz, A., Müller, T., Kandler, K. and co-authors. 2009. State of mixing, shape factor, number size distribution, and hygroscopic growth of the Saharan anthropogenic and mineral dust aerosol at Tinfou, Morocco. *Tellus* **61B**, 51–63.

Kandler, K., Schütz, L., Deutscher, C., Ebert, M., Hofmann, H. and co-authors. 2009. Size distribution, mass concentration, chemical and mineralogical composition and derived optical parameters of the boundary layer aerosol at Tinfou, Morocco, during SAMUM 2006. *Tellus* **61B**, 32–50.

Kandler, K., Schütz, L., Jäckel, S., Lieke, K., Emmel, C. and co-authors. 2011a. Ground-based off-line aerosol measurements at Praia, Cape Verde, during the Saharan Mineral Dust Experiment: Microphysical properties and mineralogy. *Tellus* **63B**, this issue.

Kandler, K., Lieke, K., Benker, N., Emmel, C., Küpper, M. and co-authors. 2011b. Electron microscopy of particles collected at Praia, Cape Verde, during the Saharan Mineral Dust Experiment: particle chemistry, shape, mixing state and complex refractive index. *Tellus* **63B**, this issue.

Kelly, W. P. and McMurry, P. H. 1992. Measurement of particle density by inertial classification of differential mobility analyzer-generated monodisperse aerosols. *Aerosol Sci. Technol.* **17**, 199–212.

Kinne, S., Lohmann, U., Feichter, J., Schulz, M., Timmreck, C. and co-authors. 2003. Monthly averages of aerosol properties: a global comparison among models, satellite data, and AERONET ground data. *J. Geophys. Res.* **108**(D20), 4634, doi:10.1029/2001JD001253.

Knippertz, P., Tesche, M., Heinold, B., Kandler, K., Toledano, C. and co-authors. 2011. Dust mobilization and aerosol transport from West Africa to Cape Verde: a meteorological overview of SAMUM-2. *Tellus* **63B**, this issue.

Leinert, S. and Wiedensohler, A. 2008. A DMA and APS based technique for measuring aerodynamic hygroscopic growth factors of micrometer-size aerosol particles. *J. Aerosol Sci.* **39**, 393–402.

Liu, B. Y. H., Pui, D. Y. H., Whitby, K. T., Kittelson, D. B., Kousaka, Y. and co-authors. 1978. The aerosol mobility chromatograph: a new detector for sulfuric acid aerosols. *Atmos. Environ.* **12**, 99–104.

Massling, A., Wiedensohler, A., Busch, B., Neusüß, C., Quinn, P. and co-authors. 2003. Hygroscopic properties of different aerosol types over the Atlantic and Indian Oceans. *Atmos. Chem. Phys.* **3**, 1377–1397.

Massling, A., Leinert, S., Wiedensohler, A. and Covert, D. 2007. Hygroscopic growth of sub-micrometer and one-micrometer aerosol particles measured during ACE-Asia. *Atmos. Chem. Phys.* **7**, 3249–3259.

Massling, A., Niedermeier, N., Hennig, T., Fors, E., Swietlicki, E. and co-authors. 2011. Results and recommendations from an intercomparison of six Hygroscopicity-TDMA systems. *Atmos. Meas. Tech.* **4**, 485–497.

Meier, J., Wehner, B., Massling, A., Birmili, W., Nowak, A. and co-authors. 2009. Hygroscopic growth of urban aerosol particles in Beijing (China) during wintertime: a comparison of three experimental methods. *Atmos. Chem. Phys.* **9**, 6865–6880.

Mészáros, A. and Vissy, K. 1974. Concentration, size distribution and chemical nature of atmospheric aerosol particles in remote oceanic areas. *J. Aerosol Sci.* **5**, 101–109.

Niedermeier, D., Wex, H., Voigtländer, J., Stratmann, F., Brüggemann, E. and co-authors. 2008. LACIS-measurements and parameterization of sea-salt particle hygroscopic growth and activation. *Atmos. Chem. Phys.* **8**, 579–590.

O'Dowd, C. D. and Smith, M. H. 1993. Physicochemical properties of aerosols over the northeast Atlantic: evidence for wind-speed-related submicron sea-salt aerosol production. *J. Geophys. Res.* **98**, 1137–1149.

O'Dowd, C. D., Smith, M. H., Consterdine, I. E. and Lowe, J. A. 1997. Marine aerosol, sea-salt, and the marine sulphur cycle: a short review. *Atmos. Environ.* **31**, 73–80.

Petters, M. D. and Kreidenweis, S. M. 2007. A single parameter representation of hygroscopic growth and cloud condensation nucleus activity. *Atmos. Chem. Phys.* **7**, 1961–1971.

Ramaswamy, V., Boucher, O., Haigh, J., Hauglustaine, D., Haywood, J. and co-authors. 2001. Radiative forcing of climate change. In: *Climate Change 2001: The scientific Basis. Contribution of Working Group I to the Third Assessment Report of the Intergovernmental Panel on Climate Change* (eds. Houghton, J. T., Ding, Y., Griggs, D. J., Noguer, M., van der Linden, P. J. and Xiasu, D.). Cambridge University Press, Cambridge, UK and New York, USA, 349–416.

Randall, D. A., Wood, R. A., Bony, S., Colman, R., Fichefet, T. and co-authors. 2007. Climate models and their evaluation. In: *Climate Change 2007: The Physical Basis. Contribution of Working group I to the Fourth Assessment Report of the Intergovernmental Panel on Climate Change* (eds. Solomon, S., Qin, D., Manning, M., Chen, Z., Marquis, M., Averyt, K. B., Tignor, M. and Miller, H. L.). Cambridge University Press, Cambridge, UK and New York, USA.

Schladitz, A., Müller, T., Kaaden, N., Massling, A., Kandler, K. and co-authors. 2009. In situ measurements of optical properties at Tinfou (Morocco) during the Saharan Mineral Dust Experiment SAMUM 2006. *Tellus* **61B**, 64–78.

Schladitz, A., Müller, T., Nordmann, S., Tesche, M., Groß, S. and co-authors. 2011. In-situ aerosol characterization at Cape Verde. Part 2: Parameterization of relative humidity- and wavelength-dependent aerosol optical properties. *Tellus* **63B**, this issue.

Stock, M., Cheng, Y. F., Birmili, W., Massling, A., Wehner, B., Müller, T., Leinert, S., Kalivitis, N., Mihalopoulos, N. and Wiedensohler, A. 2011. Hygroscopic properties of atmospheric aerosol particles over the Eastern Mediterranean: implications for regional direct radiative forcing under clean and polluted conditions. *Atmos. Chem. Phys.* **11**, 4251–4271.

Stratmann, F. and Wiedensohler, A. 1996. A new data inversion algorithm for DMPS-measurements. *J. Aerosol Sci.* **27**(**Supplement 1**), 339–340.

Swietlicki, E., Zhou, J., Covert, D. S., Hämeri, K., Busch, B. and co-authors. 2000. Hygroscopic properties of aerosol particles in the north-eastern Atlantic during ACE-2. *Tellus* **52B**, 201–227.

Swietlicki, E., Hansson, H. C., Hämeri, K., Svenningsson, B., Massling, A. and co-authors. 2008. Hygroscopic properties of submicrometer atmospheric aerosol particles measured with H-TDMA instruments in various environments-a review. *Tellus* **60B**, 432–469.

Tang, I. N. 1996. Chemical and size effects of hygroscopic aerosols on light scattering coefficients. *J. Geophys. Res.* **101**, 19245–19250.

Tang, I. N. and Munkelwitz, H. R. 1994. Water activities, densities, and refractive indices of aqueous sulfates and sodium nitrate droplets of atmospheric importance. *J. Geophys. Res.* **99**, 18801–19808.

Tesche, M., Ansmann, A., Müller, D., Althausen, D., Engelmann, R. and co-authors. 2009. Vertically resolved separation of dust and smoke over Cape Verde using multiwavelength Raman and polarization lidars during Saharan Mineral Dust Experiment 2008. *J. Geophys. Res.* **114**, D13202, doi:10.1029/2009JD011862.

Tuch, T. M., Haudek, A., Müller, T., Nowak, A., Wex, H. and co-authors. 2009. Design and performance of an automatic regenerating adsorption aerosol dryer for continuous operation at monitoring sites. *Atmos. Meas. Tech.* **2**, 417–422.

Wiedensohler, A., Orsini, D., Covert, D. S., Coffmann, D., Cantrell, W. and co-authors. 1997. Intercomparison study of the size-dependent counting efficiency of 26 condensation particle counters. *Aerosol Sci. Technol.* **27**, 224–242.